A realistic molecular model of cement hydrates

Citation: Pellenq, Roland J. -M et al. "A realistic molecular model of cement hydrates." Proceedings of the National Academy of Sciences 106.38 (2009): 16102-16107. © 2009 National Academy of Sciences

As Published: http://dx.doi.org/10.1073/pnas.0902180106

Publisher: United States National Academy of Sciences

Persistent URL: http://hdl.handle.net/1721.1/55304

Version: Final published version: final published article, as it appeared in a journal, conference proceedings, or other formally published context

A realistic molecular model of cement hydrates

Roland J.-M. Pellenq[a,b], Akihiro Kushima[c], Rouzbeh Shahsavari[b], Krystyn J. Van Vliet[d], Markus J. Buehler[b], Sidney Yip[c,d], and Franz-Josef Ulm[b,1]

[a]Centre Interdisciplinaire des Nanosciences de Marseille, Centre National de la Recherche Scientifique and Marseille Université, Campus de Luminy, Marseille, 13288 Cedex 09, France; Departments of [b]Civil and Environmental Engineering, [c]Nuclear Science and Engineering, and [d]Materials Science and Engineering, Massachusetts Institute of Technology, 77 Massachusetts Avenue, Cambridge, MA 02139

Edited by Zdeněk P. Bažant, Northwestern University, Evanston, IL, and approved July 21, 2009 (received for review February 27, 2009)

Despite decades of studies of calcium-silicate-hydrate (C-S-H), the structurally complex binder phase of concrete, the interplay between chemical composition and density remains essentially unexplored. Together these characteristics of C-S-H define and modulate the physical and mechanical properties of this ''liquid stone'' gel phase. With the recent determination of the calcium/silicon (C/S = 1.7) ratio and the density of the C-S-H particle (2.6 g/cm^3) by neutron scattering measurements, there is new urgency to the challenge of explaining these essential properties. Here we propose a molecular model of C-S-H based on a bottom-up atomistic simulation approach that considers only the chemical specificity of the system as the overriding constraint. By allowing for short silica chains distributed as monomers, dimers, and pentamers, this C-S-H archetype of a molecular description of interacting CaO, SiO_2, and H_2O units provides not only realistic values of the C/S ratio and the density computed by grand canonical Monte Carlo simulation of water adsorption at 300 K. The model, with a chemical composition of $(CaO)_{1.65}(SiO_2)(H_2O)_{1.75}$, also predicts other essential structural features and fundamental physical properties amenable to experimental validation, which suggest that the C-S-H gel structure includes both glass-like short-range order and crystalline features of the mineral tobermorite. Additionally, we probe the mechanical stiffness, strength, and hydrolytic shear response of our molecular model, as compared to experimentally measured properties of C-S-H. The latter results illustrate the prospect of treating cement on equal footing with metals and ceramics in the current application of mechanism-based models and multiscale simulations to study inelastic deformation and cracking.

atomistic simulation | mechanical properties | structural properties

By mixing water and cement, a complex hydrated oxide called calcium-silicate-hydrate (C–S–H) precipitates as nanoscale clusters of particles (1). Much of our knowledge of C-S-H has been obtained from structural comparisons with crystalline calcium silicate hydrates, based on HFW Taylor's postulate that real C-S-H was a structurally imperfect layered hybrid of two natural mineral analogs (2): tobermorite of 14-Å interlayer spacing [$Ca_5Si_6O_{16}(OH)_2.7H_20$, (3)] and jennite [$Ca_9(Si_6O_{18})(OH)_6.8H_2O$ (4)]. While this suggestion is plausible in morphological terms, this model is incompatible with two basic characteristics of real C-S-H; specifically the calcium-to-silicon ratio (C/S) and the density. Recently, small-angle neutron scattering measurements have fixed the C/S ratio at 1.7 and the density at 2.6 g/cm^3 (1), values that clearly cannot be obtained from either tobermorite (C/S = 0.83, 2.18 g/cm^3) or jennite (C/S = 1.5 and 2.27 g/cm^3). From the standpoint of constructing a molecular model of C-S-H, this means that these crystalline minerals are not strict structural analogs. Here we adopt the perspective that the chemical composition of C-S-H is the most essential property in formulating a realistic molecular description. We show that once the C/S ratio is described correctly, a number of characteristic structural features and physical properties follow naturally in atomistic simulations. We view the present model and its subsequent refinements as enabling a bottom-up perspective on the broad science of cementitious materials and the innovative engineering of concrete. Manipulation of such a testable model should ultimately allow the establishment of the critical links between nanoscale microstructure and macroscale behavior, which requires fundamental understanding of the effects of confined water in the context of creep and durability.

Model Construction. One of the key issues in designing a realistic C-S-H molecular model is the calcium-to-silicon ratio (C/S). Indeed, confirming earlier measurements by Groves et al. (6) and Richardson and Groves (7), energy dispersive X-ray analyses of C-S-H in hardened Portland cement pastes aged 1 day to 3.5 years reveal a composition variation spanning C/S from approximately 1.2 to 2.3 with a mean value of 1.7; this variation also depends on the water-to-cement (W/C) mass ratio at which cement is hydrated (5). Given the shortfalls of the natural analogs, tobermorite and jennite, to meet this compositional constraint, Richardson proposed a two-fold classification to clarify C-S-H chemistry (5). This classification references so-called tobermorite/jennite (T/J) models on one hand and tobermorite-calcium hydroxyle (T/CH) models on the other hand. The T/CH class considers models that are solid solutions of tobermorite layers sandwiching calcium hydroxide, hence providing a means to achieve a higher C/S ratio than the one of tobermorite. The T/J class considers C-S-H as an assembly of tobermorite regions followed by jennite domains. While the T/CH class was found to be relevant for hydrated KOH-activated metakaolin Portland cement, more common water activated Portland cement pastes can be only partly described by the T/J or the T/CH approaches. A realistic model for C-S-H that predicts a realistic C/S ratio thus remains a center piece of any model construction. Furthermore, quantitative information on the fractions of Si present in silicate tetrahedra with different connectivities is provided by ^{29}Si nuclear magnetic resonance (NMR) (8, 9). Such studies have established that the dimer is the most predominant of all silicate species, with the linear pentamer as the second most abundant. Tetrahedral coordination measured by NMR is expressed in terms of the Q_n factor, denoting the fractional chemical shift of a silicon atom bound to n bridging oxygens. Thus Q_o is the fraction of a single tetrahedron (a silicate monomer), Q_1 the fraction of tetrahedra at the end of a chain (a silicate dimer would have two Q_1), Q_2 the fraction of tetrahedra in the middle of a chain (a silicate pentamer would have three Q_2).

To construct a molecular model of C-S-H that has a C/S ratio consistent with small-angle neutron scattering measurements, we begin with a monoclinic periodic computational cell of dry

Author contributions: R.J.-M.P., K.J.V.V., S.Y., and F.-J.U. designed research; R.J.-M.P. and R.S. performed research; R.J.-M.P., A.K., and M.J.B. contributed new reagents/analytic tools; R.J.-M.P., A.K., R.S., S.Y., and F.-J.U. analyzed data; and R.J.-M.P., K.J.V.V., M.J.B., S.Y., and F.-J.U. wrote the paper.

The authors declare no conflict of interest.

This article is a PNAS Direct Submission.

Freely available online through the PNAS open access option.

[1]To whom correspondence should be addressed. E-mail: ulm@mit.edu.

This article contains supporting information online at www.pnas.org/cgi/content/full/0902180106/DCSupplemental.

tobermorite of interlayer spacing of approximately 11 Å, with 4, 2, and 1 units along axes *a*, *b*, and *c* with a unit cell chemical formula of $Ca_6Si_6O_{16}$. The cell contains two CaO layers lying in the *ab* plane, and eight silicate chains (2 chains each on top and bottom side of each layer). In this initial configuration the C/S ratio is 1.0; note that with this value of C/S, the layers are not electroneutral and there are interlayer calcium ions to maintain electroneutrality. We then remove SiO_2 (neutral) groups in silica tetrahedra guided by the NMR results, $Q_0 \sim 10\%$, $Q_1 \sim 67\%$, and $Q_2 \sim 23\%$ (10), obtaining a defective C-S-H structure that has a distribution of $Q_0 = 13\%$, $Q_1 = 67\%$, and $Q_2 = 20\%$, with a C/S ratio of 1.65. There are likely other ways to produce defected silicate chains that are consistent with the NMR constraints; we are currently investigating a combinatorial approach. Our procedure was carried out without the presence of any OH groups, so that a reasonable C/S ratio could be obtained under the electroneutrality constraint (11). After the silicate chain modification, we relax the dry cell using the core-shell potential model at 0 K to find a density of 2.12 g/cm^3, the interlayer distance having shifted slightly to 11.3 Å (see *Methods*). At this stage, one can observe significant distortion of the layer structure. We next performed Grand Canonical Monte Carlo simulation of water adsorption in the above defected unit cell, coupling the system to an external reservoir at a chemical potential corresponding to liquid water at 300 K (see *Methods*). At equilibrium, the adsorbed water increases the density to 2.56 g/cm^3, which is close to the experimental value provided by neutron scattering of 2.6 g/cm^3 (1). We regard this agreement, which was an outcome rather than an input or constraint to this model, to be a significant consistency check on our model development procedure. Further relaxation at 0 K of this hydrated C-S-H model yields a slight increase of the interlayer spacing from 11.3 Å to 11.9 Å, reducing the density by 4% to 2.45 g/cm^3; molecular dynamics simulations under constant pressure and temperature (NPT-MD) give the same result (see *Methods*). In the final model, one can observe water molecules adsorbed in cavities inside the calcium oxide layers as a result of relaxation. While the amount of water is similar to that present in the interlayer region of 14-Å tobermorite, the water in our model is adsorbed not only in the interlayer regions, but also in the distorted intralayer regions around the silica monomers. As a consequence of water adsorption the density increases to 2.56 g/cm^3, with the adsorbed water molecules being in an ultra-high confining environment. This water may be regarded as part of the structure, reminiscent of structural water or bound water in cement chemistry terminology. The overall chemical composition of the computational model of the hydrated C-S-H is thus found to be $(CaO)_{1.65}(SiO_2)(H_20)_{1.75}$, which is in reasonable agreement with the neutron scattering experiments $(CaO)_{1.7}(SiO_2)(H_20)_{1.8}$ (1). The molecular configuration of this model is shown in Fig. 1; and all cell parameters and atomic positions of our model are provided in the SI (see also *Methods*).

Model Validation Against Experiments. We validated the structure of our model by calculating several experimentally accessible properties. The results, summarized in Fig. 2, consist of extended X-ray absorption fine structure (EXAFS) spectroscopy signals measuring short-range order around Ca atoms (Fig. 2*A*), longer range correlations revealed in X-ray diffraction intensity (Fig. 2*B*), vibrational density of states measured by infrared spectroscopy (Fig. 2*E*), and nanoindentation measurements of elastic properties (Fig. 2*F*). The various tests provide strong evidence of a short-range structural disorder, the hallmark of a glassy phase. For instance, the simulated and experimental Ca total pair distribution functions as measured in EXASF (Fig. 2*A*), agree well, showing peaks at the same inter-atomic distances with same relative intensities that allow discriminating C-S-H against all other calcio-silicate crystalline solids (12). The fact

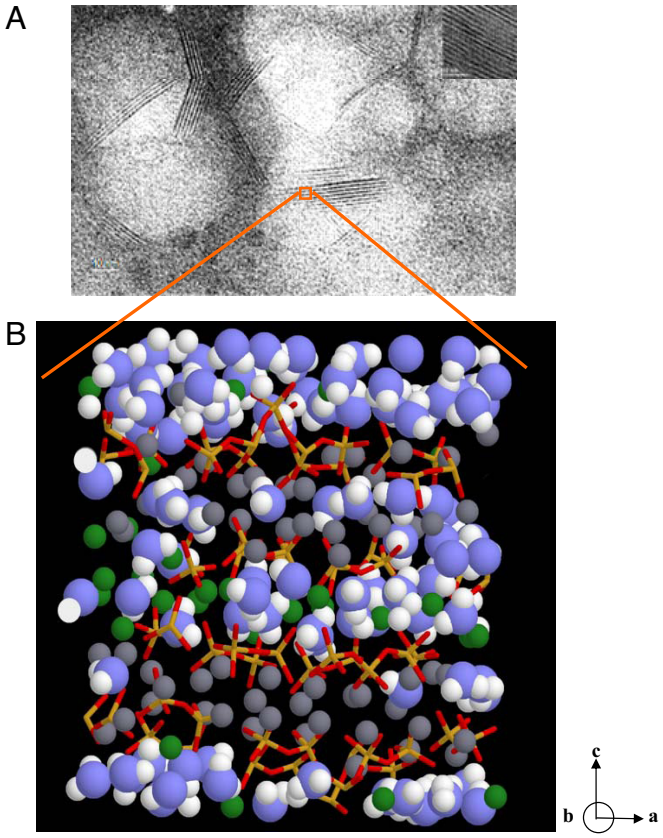

Fig. 1. (*A*) TEM image of clusters of C-S-H (courtesy of A. Baronnet, CINaM, CNRS and Marseille Université, France), the inset is a TEM image of tobermorite 14 Å from (45). (*B*) the molecular model of C-S-H: the blue and white spheres are oxygen and hydrogen atoms of water molecules, respectively; the green and gray spheres are inter and intra-layer calcium ions, respectively; yellow and red sticks are silicon and oxygen atoms in silica tetrahedra.

that the first peak in the experimental EXAFS signal is broader than that obtained in simulation suggests that real C-S-H may exhibit an even larger volume fraction of short-range structural disorder. The x-ray diffractogram of our C-S-H model (Fig. 2*B*) clearly indicates the reduced degree of crystallinity as compared with tobermorite. The suggestion that our C-S-H model can be seen as a glassy phase at short length scales is confirmed by a comparison of the partial pair distribution functions $g(r)$ of our C-S-H model with that of a true non-porous calcio-silicate glass at room temperature with the same C/S ratio and a density of 2.34 g/cm^3 (Fig. 2 *C* and *D*): the structure of the second peaks in the $g(r)$ for Si-O and Ca-O pairs in tobermorite show characteristic structural features that are absent for both the calcium-silicate glass and our C-S-H model. For the sake of consistency, the Ca-glass and crystalline tobermorite simulations were carried out with the same empirical potential model (see *Methods*), with the Ca-glass potential obtained by following the method given in (13). We may interpret this comparison to indicate that C-S-H should be considered as a glass on the short range of distances associated with the distorted intralayer structure, while retaining some layered crystal features at longer range of distances associated with the interlayer spacing.

The comparison between simulation and experimental infrared spectra (Fig. 2*E*), allows further characterization of our model. Note that calculated infrared intensities were obtained from the relaxed model C-S-H structure by performing a numerical integration over the sampled phonon modes (14). All of the experimental bands are present in the calculated spectrum

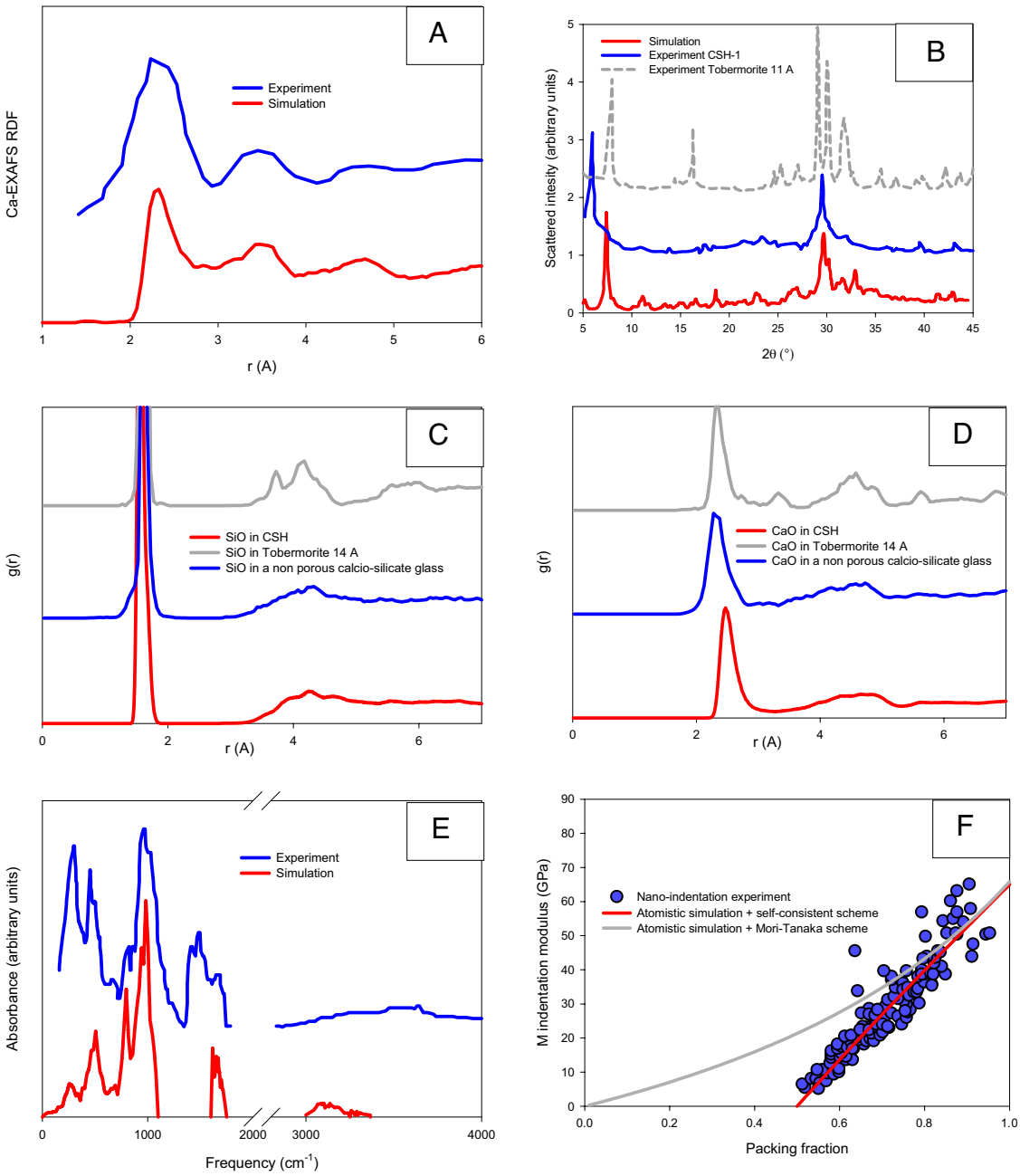

Fig. 2. Characterization and validation of molecular model of C-S-H. (*A*) EXAFS Ca-radial distribution function, exp (12). (phase shift of + 0.3 Å, background subtracted); (*B*) XRD data, exp (46). for C-S-H and (47) for tobermorite 14 Å; (*C*) SiO radial distribution function, comparison with that for a non porous calcio-silicate with Ca/Si = 1.6 and with that for tobermorite 14 Å; (*D*) idem for the CaO pair; (*E*) infrared data, exp (15); (*F*) nanoindentation data, exp (18), see text.

but the ones in the range 1,200–1,500 cm^{-1}; the absence of these bands is not surprising, as these correspond to experimental carbonation effects (Q3 silicate stretching and vibrational mode of CO_3^{2-} ions) that can be avoided in a computational model. The first low frequency band in the range 200–350 cm^{-1} corresponds to the vibration of Ca polyhedra including those of other hydration products, namely $Ca(OH)_2$ grains, that nucleate in the mesopores of the real cementitious material, in addition to C-S-H. Since our model only represents the C-S-H, this Ca polyhedra band is present in the model, but not of as high intensity as in experiment, more closely corresponding to that measured for tobermorite (15). The band in the domain 440–450 cm^{-1} can be attributed to deformations of SiO_4^- tetrahedra. The band in the range 660–670 cm^{-1} is due to Si-O-Si bending while that at 810 and 970 cm^{-1} is attributed to Si-O stretching in silica tetrahedra (Q1 and Q2 environments, respectively). Finally, infrared analysis provides some information on the nature of the water molecules: the band at approximately 1,600 cm^{-1} is characteristic of water H-O-H bending, while that at 3,300 cm^{-1} is attributed to O-H stretching. Interestingly, these band positions are lower than that of bulk liquid (bulk liquid water is also present in the mesopores of C-S-H) and are characteristic of a strong confining environment, as is also suggested from neutron quasi-elastic experiments (16).

Additionally, we consider mechanical properties of the model C-S-H, computed by stretching the cell dimensions to calculate elastic constants (Tables 1 and 2) as well as the rupture strength. For a quantitative comparison, we use nanoindentation mea-

Table 1. Elastic properties

Elastic properties	
Voigt bulk modulus in GPa	51
Reuss bulk modulus in GPa	47
Voigt shear modulus in GPa	24
Reuss shear modulus in GPa	22
Young modulus along the x-z plane in GPa	66–68
Young modulus along the y direction in GPa	55
Poisson's ratio	0.30
Plane Stress modulus in GPa	65
Strength in GPa	3

Plane stress modulus is indentation modulus.

surements that probe the stiffness and hardness of nanoscale clusters of randomly oriented C-S-H particles at the micrometer scale (Fig. 1), which have been characterized by isotropic stiffness and strength particle properties and particle packing density (17, 18). Then, using micromechanics-based scaling relations pertaining to granular (19) and porous materials (20), of the indentation elastic modulus, $M = m_s\,\Pi_M\,(\eta, \nu)$, and indentation hardness, $H = h_s\,\Pi_H\,(\eta, \alpha)$ (15, 16), we correct for the effect of interparticle porosity, via particle packing density, η, and determine the C-S-H particle indentation modulus, $m_s = E_s/(1 - \nu^2{}_s)$, and the particle hardness, h_s, (where E_s is the Young's elastic modulus, ν_s is the Poisson's ratio, α is the friction coefficient). The experimental values are in excellent agreement with the ones obtained from our computational C-S-H model, using for the elasticity constants the Reuss-Voigt-Hill average (m_s = 65 GPa, Table 1) calculated from the full elasticity tensor (Table 2) to compare with the elasticity properties of randomly oriented C-S-H particles; and for hardness the maximum negative isotropic pressure (h_s = 3 GPa, Table 1) that precedes rupture of the simulation cell perpendicular to the layer plane. These values are somewhat higher than those for 14 Å tobermorite and jennite, for which m_s = 56 GPa obtained from classical (21) and ab initio plane-wave GGA-DFT calculations (22). This comparison underscores the importance of considering a realistic C-S-H structure for the prediction of elasticity and strength properties of cement-based materials. Moreover, combining the elastic properties determined from our C-S-H model with some micromechanics models (19, 20) with no adjustable parameters, we can also probe the texture and extent of anisotropic structures within cement paste at micrometer length scales of randomly oriented C-S-H particles. Fig. 2*F* compares the prediction of two micromechanics models along with nano-indentation results; one is a porous bicontinuous matrix approach captured by the so-called Mori-Tanaka scheme (20), and the other a granular approach captured by the self-consistent scheme (19). From this comparison, we observe first that the granular approach better describes the experimental data over the entire domain of C-S-H particle packing fractions. Second, both approaches give acceptable predictions at larger packing fractions. That is, at the micrometer-scale, Mori-Tanaka and self consistent micromechanics approaches, parameterized only with nanoscale derived elasticity constants, indicate that cement paste can be conceptualized as a cohesive granular material rather than a porous bicontinuous matrix.

Table 2. Elastic tensor (Voigt notation)

C_{ij}/GPa	1	2	3	4	5	6
1	93.5	45.4	26.1	0.58	−0.05	3.46
2		94.9	30.01	−4.60	1.79	−3.00
3			68.5	−4.32	−2.72	−0.57
4				19.2	0.33	1.82
5					16.1	−0.40
6						31.2

Strength-Controlling Shear Localization. Probing atomic-level mechanisms to gain insights into structural deformation and failure at larger length scales is currently a central issue in the development of nanomechanics of hard crystalline materials (23, 24). The formulation of a molecular model of C-S-H presents an opportunity to initiate similar investigations of cementitious materials, thereby opening up a class of microstructures with unique chemistry-rich and spatially heterogeneous characteristics. A fundamental question common to all systems is the nucleation and evolution of a "unit process" in the constitutive response to tensile and shear loading, and the effects of specimen size, temperature, and strain-rate dependence. We have simulated the stress-strain behavior of our C-S-H model in affine shear deformation (strain controlled) after first relaxing the computational cell using MD at 300 K, under constant NVT ensemble conditions. A series of shear strains in increments of 0.005 is imposed; after each increment the atomic configuration is relaxed and the shear stress determined from the virial expression. Fig. 3 shows the shear stress-strain curves of the C-S-H model, as well as a "dry" version of this model in which all water molecules have been removed. The responses in both cases are a sequence of elastic loading under incremental strain, interspersed with discrete stress drops reminiscent of strain localization events. This type of intermittent or saw-tooth behavior has been observed in deformation simulation of metallic glasses (25), glassy polymers (26) as well as nanoindentation-induced dislocation nucleation (27). Further investigations of the mechanisms governing stress relaxation in this model are ongoing; here, we will discuss only the first two stress drops in each response curve. These occur at stresses between 2.5 to 3 GPa in the dry sample and approximately 1 GPa in the hydrated sample; these values are lower than the ideal shear strength, or about 10% of the shear elastic modulus, due to the defected microstructure of this C-S-H phase. Moreover, it is not surprising that the presence of water lowers the strength. On the other hand, inspection of Fig. 3*A* indicates a significant difference between the two response curves. If we take the elastic loading portion of the response after the first drop and extrapolate back to zero stress, we find a significant "residual" strain of approximately 0.1 in the dry sample, an indication of irreversible deformation associated with the first drop. In contrast, in the hydrated sample unloading after the first drop indicates essentially no residual strain, which suggests the deformation to be largely elastic. To observe the atomic displacements that correspond to these stress drops, we display in Fig. 3*B* the largest individual displacements associated with the four stress drops in Fig. 3*A*. It is clear that in the dry sample local strains are distributed across the cell, with a slight degree of strain concentration within the layers rather than in the interlayer region, especially at stage (d). It is also quite clear that in the hydrated sample the strains are localized entirely in the interlayer region and are mostly associated with displacements of water molecules. Combining these observations with the characteristics of the stress-strain response in Fig. 3*A* we can conclude that the shear response of the C-S-H model is strain localization in the interlayer region; this localization occurs in the form of sliding, ostensibly facilitated by the lubricating action of the water molecules. In the absence of water, strain localization appears to manifest as individual events of irreversible deformation. The present results demonstrate the potential to gain insights into the effects of water on the deformation behavior of the C-S-H particle. This problem bears some analogy to the phenomenon of "hydrolytic weakening" in other crystalline and glassy silicates, where it is believed that hydration causes more than a five-fold reduction in the com-

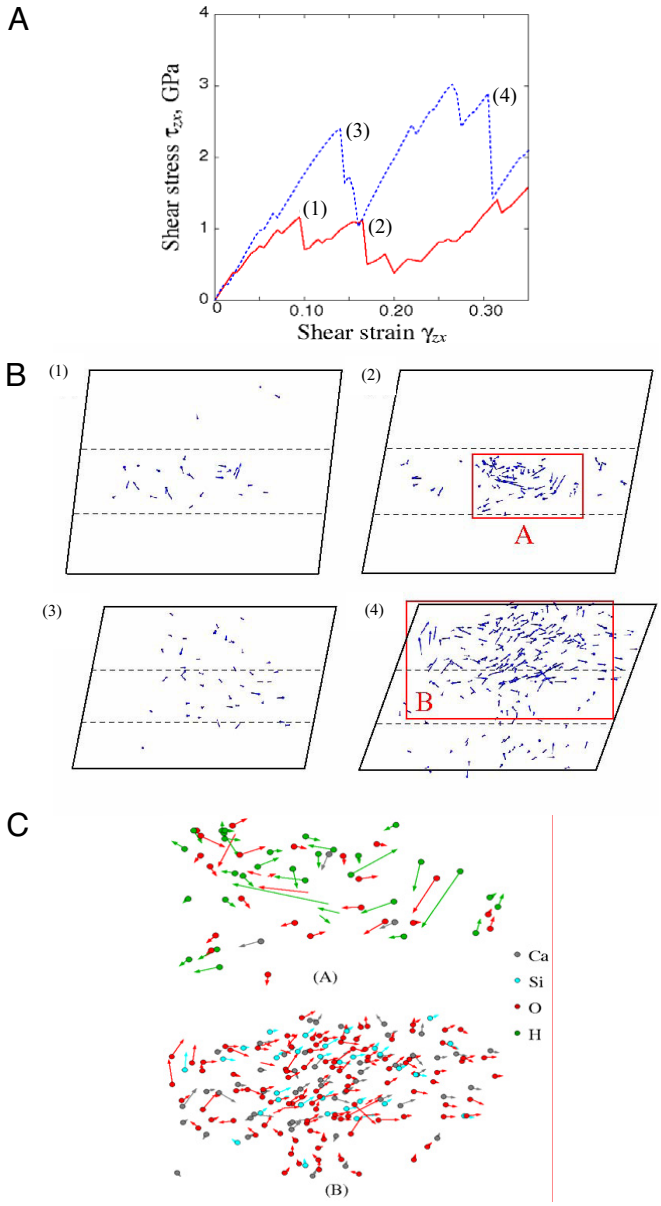

Fig. 3. (*A*) Relationships between the shear stress τ_{zx} and the strain γ_{zx} for the C-S-H model with (solid line) and without (dashed line) water molecules. (*B*) Atom displacements at the stress drops (1)–(4) in panel (*A*). Only atoms with displacement larger than 0.5 Å are shown, and the arrows indicate the displacements. Dashed lines correspond to the C-S-H layers. (*C*) Magnified view of regions (A) and (B) that are marked as red boxes in panel (*B*).

pressive strength of α-quartz (28). Simulations of water-silica interactions have identified three distinct competing mechanisms in the water attack on the siloxane bridging bond, Si-O-Si (29). Since we do not allow dissociation in our interatomic potential description, further considerations of this mechanism will be facilitated by first-principles MD studies of this C-S-H model.

In summary, our study provides an atomistic-level structural model for C-S-H, developed from a bottom-up perspective and validated against several experimental analyses of structure and properties. This model could enable many opportunities for future developments focused on understanding fundamental deformation mechanisms, diffusive properties, electrical properties and many other characteristic material parameters. C-S-H is the primary hydration product and binding phase of concrete, the synthetic material currently produced in volumes larger than any other material on Earth. The insight gained by deformation simulations based on our C-S-H model (Fig. 3) illustrates the prospect of treating cementitious composites on equal footing with less structurally complex materials. The knowledge of unit deformation mechanisms (in analogy to dislocations, shear bands, etc.) in concrete could enable the development of mechanism-based models and multiscale simulation methods to study inelastic deformation, flow, and fracture to complement and improve current empirical strength models of this complex yet ubiquitous material. The existence of an atomistic level model of the C-S-H nanostructure is crucial to enable advances in our understanding of how specific structural arrangements at the nanoscale relate to resulting material properties. In a broader context, the approach illustrated here to carry out an experimentally validated structural prediction of a complex heteronanocomposite could be applied to many other systems such as colloids, hydrated polymer or protein gels, as well as polymer nanocomposites.

Methods

From Energy Minimization to Elastic Properties Using Empirical Interatomic Potentials. All calculations were carried out with the GULP code (28–30). These calculations were performed using a set of empirical but transferable interatomic potentials calibrated on quartz and CaO compounds. Anions (here oxygens in tobermorite layers and in water molecules) were modeled as polarizable species using the core-shell model. These transferable empirical inter-atomic potentials based on the use of the formal electric charge for each interacting species, have successfully reproduced the structure and properties of many oxides (33) including silicates (34–36) and phyllosilicates (37, 38) [see reference (39) for liquid water]. The set of potentials used include two-body and three-body analytical functions that allow calculating the energy between pairs and triplets of atoms. They depend on the choice of some parameters that can be advantageously calibrated using ab initio calculations in some simple cases. Note that the calculation of electrostatic interactions between pairs of ions is carried out using the Ewald summation scheme. The advantage of such an approach compared to ab initio quantum mechanical methods is that one can compute for large systems with low symmetry, not only structural but also thermodynamic and elastic properties [from the elastic tensor using both Voigt and Reuss equations for bulk, shear, Young's, plane stress (or indentation) modulus and Poisson's ratio]. Periodic boundary conditions were used for all directions of space. Reference (40) gives all details and equations on such calculations in the case of lizardite, a layered magnesium silicate of central importance in tectonophysics. Energy minimization for finding an equilibrium structure consists in tracking stationary points that correspond to a minimum energy gradient with positive energy curvature (i.e., finding a set of atomic positions that minimizes system energy and give a Hessian operator with positive eigenvalues only). A phonon spectrum calculation at the center of the Brillouin zone is then used as a final validation from which one obtains the list of lattice vibration frequencies that should be all positive except the first three that should be zero (unit cell translational invariance). Such minimization procedure gives a zero temperature solution. In this work, all degrees of freedom were considered including atomic positions, unit cell dimensions and angles. All potential mathematical form and parameters are given in the SI. The same approach but at fixed volume was used to perform deformation and shear calculations: all atomic degrees of freedom were allowed to relax for a given cell volume modifying one cell parameter at a time. The derivative of the system energy versus the incremental modified cell parameter (the interlayer distance) is used to calculate the cohesive pressure that can be compared with experimental nanoindentation data (17, 18). Numerical shear experiments were carried out with the same strategy by modifying at each step a cell angle parameter, then followed by molecular dynamics simulation in the Canonical Ensemble (i.e., at constant volume, see below).

The Grand Canonical Monte Carlo Technique for Water Adsorption. In this work, we first produced an anhydrous version of the C-S-H substrate and subsequently calculated the maximum amount of water that can be accommodated in its pore voids. For this purpose, we used the Grand Canonical Monte Carlo (GCMC) simulation technique that is well-suited to study adsorption/desorption processes. GCMC simulations involve the determination of the properties of a system at constant volume V (the pore with the adsorbed phase) in equilibrium with a

fictitious infinite reservoir of particles imposing its chemical potential μ and its temperature T (41, 42). For different values of μ, the absolute adsorption isotherm can be determined as an ensemble average of the adsorbed atom numbers in the system versus the pressure of the gas reservoir P (the latter can be obtained from the chemical potential according to the equation of state for the bulk gas). The adsorption and desorption processes can be respectively simulated by increasing or decreasing the chemical potential of the reservoir; the final configuration of a simulation is the initial state for the next point. Periodic boundary condition was used in all directions of space as for the energy minimization procedure. An equal number of attempts for translation, rotation, creation or destruction of molecules was chosen. The isotherm was calculated for 300 K. Acknowledging the very restricted available space in between tobermoritic layers, one should not expect capillary condensation to occur in contrast to larger pore systems such as vycor (43). In our case, the adsorption/desorption process is expected to be close to that observed for microporous zeolite as far as water adsorption is concerned (44). We did not calculate the entire water adsorption/desorption isotherm, but performed a single GCMC simulation with the water chemical potential fixed to a value that corresponds to the bulk liquid phase with a density of 1 g/cm^3 at room temperature ($\mu = 0$ eV for the used water potential model; note that the water-oxygen atomic shells were switched-off and water molecules and substrate were treated as rigid bodies during the GCMC procedure). A complete study of the state of water confined in our realistic model of C-S-H including thermodynamics and dynamics properties will be presented in a separate publication.

NVT and NPT Molecular Dynamics . Room temperature relaxation and deformation were carried out using molecular dynamics simulation in the NPT and NVT statistical ensembles integrating motion equations with the leapfrog Verlet algorithm with Nosé-Hoover thermostat and pressiostat (with the default GULP parameters for each of these constraints). When relaxing in NPT conditions (with zero external pressure) the resulting system from energy minimization, the simulation considers finite temperature entropic effects.

X-Ray Diffraction. X-ray diffraction patterns were calculated with the CRYSTALDIFFRACT code as part of the CRYSTAL-MAKER package www.crystalmaker.com/crystaldiffract/ at a wave length of 1.54 Å and an apparatus aperture broadening of 0.4 Å^{-1}.

Reproducibility of Results. Details for the calculation including the interatomic potential functions and related parameters, as well as details on the numerical strategy and simulation techniques used, and the final atomistic model (and relevant coordinates) are provided in the SI to this manuscript. A file containing all of the atomic coordinates is available upon request to RJM Pellenq (pellenq@mit.edu) or FJ Ulm (ulm@mit.edu).

ACKNOWLEDGMENTS. We thank Cimpor Corporation, Portugal, for support of the ''Liquid Stone'' project, enabled through the MIT-Portugal program. We thank Dr. P. Ganster and Prof A. Baronnet (CINaM, CNRS-Marseille Université, France) for making available to us respectively the calcio-silicate glass atomistic model and the transmission electron microscopic image of C-S-H.

1. Allen AJ, Thomas JJ, Jennings HM (2007) Composition and density of nanoscale calcium-silicate-hydrate in cement. *Nat Mater* 6:311–316.
2. Taylor HFW (1993) Nanostructure of CSH, current status. *Adv Cem Bas Mat* 1:38–46.
3. Bonaccorsi E, Merlino S, Kampf AR (2005) The crystal structure of tobermorite 14 A (Plombierite), a C-S-H phase. *J Am Ceram Soc* 88:505–512.
4. Bonaccorsi E, Merlino S, Taylor HFW (2004) The crystal structure of jennite, $Ca_9Si_6O_{18}(OH)_6$ $8H_2O$. *Cem Conc Res* 34:1481–1488.
5. Richardson IG (1999) The nature of C-S-H in hardened cements. *Cem Concr Res* 29:1131–1147.
6. Groves GW, Le Sueur PJ, Sinclair W (1986) Transmission electron microscopy and microanalytical studies of ion-beam-thinned sections of tricalcium silicate paste. *J Am Ceram Soc* 69:353–356.
7. Richardson IG, Groves GW (1992) The microstructure and microanalysis of hardened cement pastes involving ground granulated blast-furnace slag. *J Mater Sci* 27:6204–6212.
8. Cong X, Kirkpatrick RJ (1996) Si-29 MAS NMR study of the structure of calcium silicate hydrate. *Adv Cem Bas Mat* 3:144–156.
9. Ayuela A, et al. (2007) Silicate chain formation in the nanostructure of cement-based materials. *J Chem Phys* 127:164710.
10. d'Espinose de la Caillerie J-B, Lequeux N (2008) Lecture on the structure of CSH, AFm and AFt phases. In *Physique*, *Chimie et Mécanique des Matériaux Cimentaire*, eds Ecole ATILH-CNRS, 3rd Ed.
11. Richardson IG (2004) Tobermorite/jennite and tobermorite calcium hydroxide-based model for the structure of CSH: Applicability to hardened pastes of tricalcium silicate, β-dicalcium silicate, Portland cement and bends of Portland cement with blast furnace slag, metakaolin or silica fume. *Cem Conc Res* 34:1733–1777.
12. Lequeux N, Moreau A, Philippot S (1999) Extended X-ray absorption fine structure investigation of calcium silicate hydrates. *J Am Ceram Soc* 8:1299–1306.
13. Ganster P, Benoit M, Kob W, Delaye JM (2004) Structural properties of a calcium aluminosilicate glass from molecular-dynamics simulations: A finite size effects study. *J Chem Phys* 120:10172–10181.
14. Dowty E (1987) Fully automated microcomputer calculation of vibrational spectra. *Phys Chem Miner* 14:67–79.
15. Yu P, Kirkpatrick RJ, Poe B, McMillan PF, Cong X (1999) Structure of calcium silicate hydrate (C-S-H): Near-, mid-, and far-infrared spectroscopy. *J Am Ceram Soc* 82:742–748.
16. Fratini E, Chen S-H, Baglioni P, Bellissent-Funel M-C (2001) Age-dependent dynamics of water in hydrated cement paste. *Phys Rev E* 64:020201.
17. Constantinides G, Ulm F-J (2007) The nanogranular nature of C–S–H. *J Mech Phys Solids* 55:64–90.
18. Ulm F-J, Vandamme M, Bobko C, Ortega JA, Tai K, Ortiz C (2007) Statistical indentation techniques for hydrated nanocomposites: Concrete, bone, and shale. *J Am Ceram Soc* 90:2677–2692.
19. Hershey AV (1954) The elasticity of an isotropic aggregate of anisotropic cubic crystals. *J Appl Mech* 21:135–144.
20. Mori T, Tanaka K (1973) Average stress in matrix and average elastic energy of materials with misfitting inclusions. *Acta Metall* 21:1605–1609.
21. Pellenq RJ-M, Van Damme H (2004) Why does concrete set? The nature of cohesion forces in hardened cement-based materials. *MRS Bull* 29:319–232.
22. Shahsavari R, Buehler MJ, Pellenq RJ-M, Ulm F-J (2009) First-principles study on elastic constants and interlayer interactions of complex hydrated oxides: The case study of tobermorite and jennite. *J Am Ceram Soc*, 10.1111/j.1551-2916.2009.03199.x.
23. Suresh S, Li J (2008) Deformation of the ultra-strong. *Nature* 456:756.
24. Zhu T, Li J, Ogata S, Yip S (2009) Mechanics of ultra-strength materials. *MRS Bulletin* 34:167–172.
25. Argon AS, Demkowicz M (2008) What can plasticity of amorphous silicon tell us about plasticity of metallic glasses? *Metall Mater Trans A* 39:1762.
26. Mott PH, Argon AS, Suter UW (1993) Atomistic modeling of cavitation of glassy polymers. *Phil Mag A* 68:537.
27. Li J, Van Vliet KJ, Zhu T, Yip S, Suresh S (2002) Atomistic mechanisms governing elastic limit and incipient plasticity in crystals. *Nature* 418:307.
28. Griggs D (1974) A model of hydrolytic weakening in quartz. *J Geophys Res* 79:1653.
29. Zhu T, Li J, Lin X, Yip S (2005) Stress-dependent molecular pathways of silica-water reaction. *J Mech Phys Solids* 53:1597.
30. Gale JD (1996) Empirical potential derivation for ionic materials. *Phil Mag B* 73:3–19.
31. Gale JD (1997) GULP: A computer program for the symmetry-adapted simulation of solids. *J Chem Soc Faraday Trans* 93:629–637.
32. Gale JD, Rohl AL (2003) The general utility lattice program (GULP). *Mol Sim* 29:291–341.
33. De Leeuw NH, Watson JW, Parker SC (1995) Atomistic simulation of the effect of dissociative adsorption of water on the surface-structure and stability of calcium and magnesium-oxide. *J Phys Chem* 99:17219–17225.
34. Dove MT, Cool T, Palmer DC, Putnis A, Salje EKH, Winkler B (1993) On the role of Al-Si ordering in the cubic-tetragonal phase transition of Leucite. *Am Mineral* 78:486–492.
35. De Leeuw NH, Du ZM, Li J, Yip S, Zhu TJ (2003) Computer modeling study of the effect of hydration on the stability of a silica nanotube. *Nanoletters* 3:1347–1352.
36. Winkler B, Dove MT, Leslie M (1991) Static lattice energy minimization and lattice-dynamics calculations on aluminisilicate minerals. *Am Mineral* 76:313–331.
37. Collins DR, Catlow CRA (1992) Computer simulation of structures and cohesive properties of micas. *Am Mineral* 77:1172–1181.
38. Saint-Diaz CI, Laguna-Hernandez A, Dove MT (2001) Modeling of dioctahedral 2 : 1 phyllosilicates by means of transferable empirical potentials. *Phys Chem Min* 28:130–141.
39. De Leeuw NH, Parker SC (1998) Molecular-dynamics simulation of MgO surfaces in liquid water using a shell-model potential for water. *Phys Rev B* 58:13901–13908.
40. Auzende A-L, Pellenq RJ-M, Devouard B, Baronnet A, Grauby O (2006) Atomistic calculations of structural and elastic properties of serpentine minerals: The case of lizardite. *Phys Chem Min* 33:266–275.
41. Nicholson D, Parsonage NG (1982) in *Computer Simulation and the Statistical Mechanics of Adsorption* (Academic, New York).
42. Frenkel D, Smit B (2002) in *Understanding Mol Simul* Academic (New York), 2nd Ed.
43. Puibasset J, Pellenq RJ-M (2005) Water adsorption in disordered mesoporous silicaVycor at 300 K and 650 K: A Grand Canonical Monte Carlo simulation study of hysteresis. *J Chem Phys*, 122:094704.
44. Puibasset J, Pellenq RJ-M (2008) Grand Canonical Monte Carlo simulation study of water adsorption in silicalite at 300 K. *J Phys Chem B* 112:6390–6397.
45. Richardson IG (2008) The calcium silicate hydrates. *Cem Conc Res* 38:137–158.
46. Janika JA, Kurdowsk W, Podsiadey R, Samset J (2001) Fractal structure of CSH and tobermorite phases. *Acta Phys Polonic* 100:529–537.
47. Martin SI (1994) Synthesis of tobermorite: A cement phase expected under repository conditions. Lawrence Livermore National Laboratory Report, November (http://www.osti.gov/bridge/servlets/purl/25005–1emzmW/webviewable/25005.pdf and http://www.osti.gov/bridge/servlets/purl/25005–1emzmW/webviewable/25005.pdf).